Strong Increase of Thawing of Subsea Permafrost in the 22nd Century Caused by Anthropogenic Climate Change

Stiig Wilkenskjeld[1], Frederieke Miesner[2], Paul P. Overduin[2], Matteo Puglini[1,3,*], and Victor Brovkin[1,4]

[1]Max Planck Institute for Meteorology, Hamburg, Germany.
[2]Alfred Wegener Institute Helmholz Center for Polar and Marine Research, Potsdam, Germany.
[3]Université Libre Bruxelles, Bruxelles, Belgium.
[4]CEN, University of Hamburg, Hamburg, Germany.
[*]No longer active in science.

Correspondence: Corresponding author: S. Wilkenskjeld, Land in the Earth System, Max Planck Institute for Meteorology, Bundesstraße 53, D-20146 Hamburg, Germany
(stiig.wilkenskjeld@mpimet.mpg.de)

Abstract.

Most Earth System Models (ESMs) neglect climate feedbacks arising from carbon release from thawing permafrost, especially from thawing of sub-sea permafrost (SSPF). To assess the fate of SSPF in the next 1000 years, we implemented SSPF
5 into JSBACH, the land component of the Max Planck Institute Earth Model (MPI-ESM). This is the first implementation of SSPF processes in an ESM-component. We investigate three extended scenarios from the 6th phase of the Coupled Model Intercomparison Project (CMIP6). In the 21st century only small differences are found among the scenarios, but in the upper-end emission scenario SSP5-8.5, especially in the 22nd century SSPF ice melting is more than 15 times faster than in the preindustrial period. In this scenario about 35% of total SSPF volume and 34% of SSPF area is lost by year 3000 due to climatic
10 changes. In the more moderate scenarios, the melting maximally exceeds the preindustrial rate by a factor of 4 and the climate change induced SSPF loss (volume and area) by year 3000 does not exceed 14%. Our results suggest that the rate of melting of SSPF ice is related to the length of the local open water season, and thus that the easily observable sea ice concentration may be used as a proxy for the change of SSPF.

15 # 1   Introduction

More than 1300 Pg carbon are stored in the permafrost soils (perennially frozen soils) of the Arctic (Hugelius et al., 2014). During the present interglacial period, the holocene, microbiological activity in partial thawed soils degraded a fraction of the stored organic carbon and released it to the atmosphere. Enhanced warming during the Anthropocene has in recent years accelerated this carbon release (Schuur et al., 2015). Most studies have been focused on the thawing of the terrestrial per-

mafrost (Koven et al., 2015; Kleinen and Brovkin, 2018; Turetsky et al., 2020). Since the Last Glacial Maximum (LGM) about $3.5 \cdot 10^6 \ km^2$ (Sayedi et al., 2020) of permafrost soils were submerged by the sea level rising by about $120 \ m$. These submerged permafrost sediments (sub-sea permafrost, SSPF) now form the major part of the Arctic Shelf. Since the benthic temperatures are above the freezing point and their interannual variability small, the submergence below sea water causes a slow but continuous thawing of the submerged permafrost sediments from the top. Sayedi et al. (2020) suggest that about $500 \ Pg$ carbon in the form of organic carbon and methane gas may be trapped in the SSPF and become available for microbial decomposition as SSPF thaws. This estimate is however highly uncertain due to the sparsity of measurements (Schuur et al., 2015).

The quantitative projection of the future climate is often done using Earth System Models (ESMs) which include the carbon cycle. However, among the ESMs participating in the 6th phase of the Coupled Model Intercomparison Project (CMIP6, Eyring et al. (2016)) only few include the dynamics of the terrestrial permafrost (Lawrence et al., 2019) and none of them included subsea permafrost (SSPF). These models thus lack potentially important feedbacks from the carbon cycle on the global climate. Several modelling studies have aimed at projecting the fate of terrestrial permafrost (Kleinen and Brovkin (2018), McGuire et al. (2018)). A few studies hindcasted subsea permafrost regionally (Shakhova et al. (2009), Nicolsky and Shakhova (2010), Nicolsky et al. (2012), Angelopoulos et al. (2019)) or at the pan-Artic scale (Overduin et al., 2019). Extrapolating observed temperature trends, Dmitrenko et al. (2011) constructed a future scenario for the SSPF in the Laptev Sea and on the East Siberian Shelf. In this study we present the first steps to include subsea permafrost in the Max Planck Institute Earth System Model (MPI-ESM) to investigate the magnitude of SSPF—climate feedbacks in the future. We explore the possible range of pan-Arctic SSPF thawing by applying climate forcings from several CMIP6 scenarios to the Arctic SSPF areas.

2 Methods

The land model JSBACH (Reick et al., 2013; Brovkin et al., 2013) is the land component of the MPI-ESM (Giorgetta et al., 2013). The JSBACH version in the MPI-ESM 1.2 (Mauritsen et al., 2019) includes a multilayer soil hydrology (Hagemann and Stacke, 2015) and the multi-compartment soil carbon model YASSO (Tuomi et al., 2009; Goll et al., 2015). The version used in this study was extended with a model for freezing soil water (Ekici et al., 2014), the dynamical inundation model TOPMODEL (Beven and Kirkby, 1979; de Vrese et al., 2021) and a methane release model (Riley et al., 2011) as described in Kleinen et al. (2020). de Vrese et al. (2021) furthermore added vertically layered soil carbon to study the organic soil development in permafrost regions. Still modifications were needed to be able to simulate SSPF.

2.1 Submerging

To implement SSPF processes in an ESM land model, it is necessary to consider both land and subsea points which experience very different boundary conditions and have different active processes.

For the subsea points MPI-OM, the ocean component of MPI-ESM, benthic temperatures were used as an upper boundary condition instead of atmospheric temperatures as are used for terrestrial points. For sub-sea points, the radiative and hydrolog-

ical forcings were switched off. The sediment pore space is assumed to be constantly filled with a mixture of water and ice and there is no advection of water.

Plant growth and phenology were disabled for sub-sea points, leaving these points with a thermally active and carbon-decomposing sediment model.

2.2 Geothermal heat flux

In most experiments JSBACH was forced by a geothermal heat flux from beneath. The geothermal heat flux was based on the geologically based data set presented in Davies (2013). This data set was processed for the SuPerMAP model (Overduin et al., 2019) and converted from a flux (units $W\,m^{-2}$) to a geothermal temperature gradient (units $K\,m^{-1}$) assuming the average heat conductivity of the sediment/soil/rock/water/ice mixture of the lowest layers (i.e. low porosity) to be the same as that of the JSBACH bedrock: $2\,W\,K^{-1}\,m^{-1}$. The resulting pan-Arctic geothermal temperature gradient (Fig. S1) ranges from $19\,mK\,m^{-1}$ to $115\,mK\,m^{-1}$ (average $35\,mK\,m^{-1}$). A consequence of this implementation is that the temperature of the lowest model layer, layer n, cannot change arbitrarily. For each model point $T_n = T_{n-1} + \frac{d_{n-1}+d_n}{2}GG$, where T_i and d_i are the temperature and thickness of layer i respectively, n the number of vertical layers and GG is the geothermal temperature gradient.

2.3 Salinity

SuPerMAP incoperates salt into the newly deposited sediments during periods when the considered model points are inundated into the ocean, i.e. during the interglacials (Overduin et al., 2019). Since the model points have individual inundation histories, the sediments thus have horizontally and vertically variable salinities. The salt distribution from SuPerMAP was preserved in JSBACH in the form of a local freezing point depression: $T_{melt} = -0.054\,K\,kg\,g^{-1}\,S$, where S is the salinity in units of $g\,kg^{-1}$. Diffusion of salt as modelled by e.g. Angelopoulos et al. (2019); Malakhova and Eliseev (2020) is a very slow process (Harrison and Osterkamp (1978) reports a diffusion coefficient for salinity about 4 orders of magnitude lower than for temperature). Due to the compartively short time scale covered in the present study diffusion of salt was not implemented. We refer to "SSPF" only when the sediments are frozen, i.e. it is not sufficient to have sub-zero temperatures.

The lack of salt diffusion causes the model artefact, that the porewater may freeze if it is submerged under (saline) liquid sub-zero-temperature seawater, whereas in reality this porewater would, though diffusive exchange with the overlying seawater, be sufficiently saline to prevent freezing. To prevent this buffering of energy in a non-physical re-freezing of the pore water in the upper layers, the active freezing of porewater was disabled for sub-sea points. Additional experiments were performed to test the consequences of this hypothesis.

2.4 Model setup and experiments

JSBACH was run on the T63 horizontal grid with a resolution of $\approx 1.9 \times 1.9$ degrees or $\approx 50 \times 200\,km$ at the Arctic latitudes around $75°N$ where most of the SSPF is found. In this setup, 407 points are located on the modern Arctic shelf at a distance

of $\leq 20\,km$ from a point in the SuPerMAP model (Overduin et al., 2019). In the SuPerMAP setup, points with water with depths $< 150\,m$ were selected since these potentially hold SSPF. In this JSBACH setup a sub-sea point on average represents an area of about $11{,}400\,km^2$. Vertically, 22 layers were used to represent the upper $1000\,m$ of sediment with layer thicknesses

85   between $6.5\,cm$ and $300\,m$. Generally the layer thickness increases exponentially with increasing depth, but additional layers were added to the depth range $0.5 - 3\,m$. This vertical setup is a downward extension of the 18 soil layer model used by de Vrese et al. (2021).

Sediment porosity and water depth were adopted from the SuPerMAP points used. The porosity decreases exponentially with increasing depth from ≈ 0.4 in the upper layer to ≈ 0.1 in the lowest and is the same for all geographical points.

90   Experiments were conducted following each of the three CMIP6 SSP scenarios SSP1-2.6, SSP2-4.5 and SSP5-8.5 to evaluate the fate of SSPF ice in scenarios with low, intermediate and upper-end future global warming, respectively.

Since SSFP is never in equilibrium with the boundary conditions, two additional control experiments were conducted, referring to a preindustrial and a present day climate respectively. These two experiments are used to assess SSPF thawing in a hypothetical world without anthropogenic climate change and were cyclically forced with 24 years of forcing data from 1850-

95   1873 (preindustrial) and 1986-2009 (present day) respectively. Further experiments were performed to assess the consequences of some of the model assumptions.

Each of the performed experiments (table 1) cover at least the period 1850 to 3000 with the exception of the present-day control simulation which branches off from SSP1-2.6 in 2010 and thus covers only the years 2010 to 3000. The three main experiments, *pmt_ssp126*, *pmt_ssp245* and *pmt_ssp585* are identical for the period 1850 to 2009.

2.5 Initial conditions

100

The model was initialized with sediment ice content, temperature and salinity from SuPerMAP (Overduin et al., 2019). For each point the data from the SuPerMAP point nearest to the center of the respective JSBACH cell was used.

To avoid an initial shock arising from differences between the SuPerMAP and JSBACH models, SuPerMAP was rerun for these points from the LGM ($23.5\,ka\,BP$) using a linear interpolation between the idealized benthic temperatures (ranging

105   from -1.8 to 0^oC dependent on water depth, see Overduin et al. (2019) for details) and the temporal average of the MPI-ESM CMIP6 preindustrial benthic temperatures, defined as the period $1850 - 1873$. The interpolation was ended $1\,ka\,BP$, so that, for the last 1000 years, SuPerMAP was forced solely with the preindustrial temperatures.

The SuPerMAP output at $2\,m$ vertical resolution, was assumed to be valid at the layer midpoint and interpolated linearly to the JSBACH layers. For JSBACH layers above $1\,m$, the values for the upper SuPerMAP layer were assumed representative.

110   Since the seasonal temperature cycle penetrates further down (Fig. S12), the results are not sensitive to this initial assumption.

The ice saturations given by SuPerMAP were converted to "ice column lengths" for each layer i according to $ice_i = \frac{sat_i}{por_i d_i}$ where ice_i is the ice column length, sat_i is the ice saturation, por_i the porosity and d_i the layer thickness. The initial ice column length accumulated over all layers (Fig. 1, left panel) ranges from 0 to over $180\,m$. The initial area of SSPF is $\approx 2.89\cdot10^6\,km^2$ (242 of the 407 points) where $\approx 0.77\cdot10^6\,km^2$ is less than $10\,m$ thick. The total initial ice volume is $\approx 153\cdot10^3\,km^3$. Vertically,

115   the ice saturation (Fig. 1, right panel), is highest at $\approx 6\,m$ depth with a secondary peak at $\approx 75\,m$. The SSPF ice saturation is

closely anticorrelated with the embedded salt, consistent with the freezing point depression and the inundation history of the last two glacial cycles.

2.6 Boundary conditions

The sub-sea points of JSBACH were forced with monthly mean benthic temperatures as upper boundary conditions. These were adopted from the MPI-ESM runs presented in detail in Kleinen et al. (2021) extending the CMIP6 scenarios beyond year 3000. Until year 2500 these runs were forced by the CO_2 concentration scenarios presented in Meinshausen et al. (2020). After year 2500 MPI-ESM was forced by output of the intermediate complexity climate model CLIMBER-2 (Brovkin et al., 2012; Kleinen et al., 2016; Petoukhov et al., 2000). The benthic data were interpolated from the MPI-OM GR30 grid onto the T63 grid using *CDO remapcon* (Schulzweida, 2019). The forcing of the different scenarios diverge from 2010 onward (not from 2016 as described in the CMIP6 protocol (Eyring et al., 2016)) for technical reasons (see Kleinen et al. (2021)).

Three scenarios were used: SSP1-2.6, SSP2-4.5 and SSP5-8.5. In all scenarios the benthic temperature rises from around year 2000 and stabilizes at a new essentially constant level (Fig. S5). In SSP1-2.6 the rise only lasts a few decades and is in total $< 1\,K$, in SSP2-4.5 the temperature in total rises $\approx 2\,K$, mainly before year 2150. For these scenarios, the largest temperature increases are found in the Barents Sea and Baffin Bay (Fig. S6), where not much SSPF ice is found (Fig. 1, left). The SSP5-8.5 benthic temperature in total rises almost $10\,K$ with the strongest trend in the 22nd century (Fig. S5). For the individual model points the increase is between 7 and $16\,K$, highest in Baffin Bay and lowest in the Laptev Sea (Fig. S6, right). In all scenarios the benthic temperatures increase less than average for points which contain SSPF and the highest temperature rise is found in coastal waters.

3 Results

The amount of SSPF ice decreases smoothly over the entire experiment period (Fig. 2) in all scenario and control experiments, however at very different rates. In the experiment forced with a preindustrial forcing (*pmt_pre*) ice melts at an essentially constant rate of $\approx 7.5\,km^3\,a^{-1}$ over the entire period. Virtually same behaviour at rates of 9.1 and $11.7\,km^3\,a^{-1}$ is seen in the present day (*pmt_curr*) and SSP1-2.6 (*pmt_ssp126*) experiments, respectively. The experiments forced with the two SSPs with stronger warming, *pmt_ssp245* and *pmt_ssp585*, result in an accelerating ice-melting from the present day to 50–100 years in the future, and thereafter slowly decreasing melting rates. The average melting rate for the *pmt_ssp245* is $17.7\,km^3\,a^{-1}$ and thus not too much higher than for the stabilization scenarios, *pmt_curr* and *pmt_ssp126*. However, the *pmt_ssp585* has an average melting rate of $54.6\,km^3\,a^{-1}$ and thus on average more than 3 times as much ice is lost, even compared to the intermediate forcing scenario *pmt_ssp245*. The difference between the scenarios is minor in the 21st century, but the melting increases dramatically the 22nd in the *pmt_ssp245* simulation and much more so in the *pmt_ssp585* simulation. During this century the average melting in *pmt_ssp585* exceeds that of the control run (*pmt_pre*) by a factor of 15.8 (Fig. 3), $116\,km^3\,a^{-1}$ of ice is lost. *pmt_ssp245* melts 3–5 times more than the control. This ratio drops again to about 7 and 2 for the two scenarios respectively and even further in the far future beyond 2500. In *pmt_ssp126* and *pmt_ssp245* the main melting takes place on the

shelf of the Kara sea (Fig. 4) whereas in *pmt_ssp585* the main ice loss is on the shelves of the Laptev and East Siberian Seas. In agreement with earlier findings (Overduin et al., 2012, 2019; Angelopoulos et al., 2019), the largest melting is found near

150   the coast, where the water is shallowest and the submerging took place most recently. Thawing in these regions was initiated comparatively recently, and thus the ice-bonded permafrost table (IBPT) is still close to the sediment-water interface.

By the year 3000 the initial area of SSPF ($2.89 \cdot 10^6 \, km^2$) is reduced to $2.63 \cdot 10^6 \, km^2$, $2.55 \cdot 10^6 \, km^2$, $2.37 \cdot 10^6 \, km^2$, $2.22 \cdot 10^6 \, km^2$ and $1.65 \cdot 10^6 \, km^2$ for the two control runs and the three SSPs, respectively. The disproportional large loss of SSPF area between 1850 and 2100 (Table 2) compared to the volume loss is explained by the rather large area of thin SSPF

155   ice ($0.77 \cdot 10^6 \, km^2$ has $< 10 \, m$ of ice). In general, the relative loss of SSPF area is larger than that of SSPF volume, most pronounced for the intermediate scenario experiments *pmt_ssp126* and *pmt_ssp245*. The two control experiments (*pmt_pre* and *pmt_curr*) apply a cyclic forcing which means that there are no long term geographical shifts in the benthic temperatures. This leads to essentially fixed area to volume melting ratio.

Initially the highest SSPF ice saturation ($\approx 86\%$, Fig. 1b) is found in a layer around $6 \, m$ depth. In all main experiments the

160   ice saturation of this layer is reduced from about 2050 onwards (Fig. 5), but to a very different degree. In *pmt_ssp1-2.6* and *pmt_ssp2-4.5* it is reduced to a saturation of $\approx 55\%$ and $\approx 30\%$ in year 3000 respectively, whereas in *pmt_ssp5-8.5* the ice at this depth is completely melted shortly after year 2100. This layer effectively insulates the deeper ice and thus prevents ice melting in the deeper layers. In *pmt_ss585* the IBPT quickly deepens after year 2100 and reaches a depth of $\approx 100 \, m$ before year 2500. The melting rate of SSPF ice however decreases during this period due to the lower concentrations of SSPF ice

165   between 6 and $100 \, m$ depth.

SSPF ice is melted from below by geothermal heat in addition to the climatically driven melting from the above. All ice in the lowest layer (layer 22, center at $850 \, m$ depth, initially $0.69 \, \%$ saturated) is gone by year 3000, and in layer 21 (center depth $550 \, m$) the ice saturation decreases from an initial $14.5 \, \%$ to $12.2 \, \%$ in year 3000. Effects of geothermal heat flux are also seen in the above layer(s), but in these layers the melting is caused by a combination of heat from below (geothermal) and above

170   (climate).

The development of melting and temperature for a selected section across the East Siberian Shelf in *pmt_ssp585* is illustrated in detail in Fig. 6, where 7 time slices of (upper panel) SSPF ice saturation and sea ice concentration (SIC) and sediment and air temperature changes (lower panel) are shown. Before year 2200 salinity-induced taliks (unfrozen lenses) are found in the layers centered at $38 \, m$ and $150 \, m$. By year 2100 only a little ice at $2 - 3 \, m$ depth is melted away and the temperature at the

175   same depths rises by $\approx 2 \, K$ preferentially towards the coast. In the 22nd century a dramatic rise in temperature of $> 8 \, K$ in the sediments above $\approx 5 \, m$ is associated with melting of all ice above $10 \, m$. As long as sea ice is present (until about 2100) the temperature rise in the upper sediments is decoupled from the atmospheric temperature rise. After the disappearance of the sea ice, the temperature rise of upper sediments and atmosphere are closely linked together.

The insulating, and thus SSPF preserving, effect of sea ice can also be observed on the pan-Arctic scale (compare Figs. S2,

180   S3 and S5). In the 19th and early 20th century the annual mean SIC of the SSPF area is 74% (68% of the modelled area, Fig. S2), rapidly dropping in the first half of the 21st century. In SSP1-2.6 this is followed by a slight rise until about 2200 and a stabilization at $> 50\%$. SSP2-4.5 also stabilizes though below 40% after a drop at a lower rate until about 2150. In SSP5.8-5

the sea ice continues to shrink at a fast rate and is entirely gone at the end of the 21st century except from seasonal ice in the coastal waters of the Laptev sea. Thus, from this point in time also at pan-Arctic scale, the benthic temperature (S5) start to

185 adapt to the higher atmospheric temperatures (Fig. S3).

The melting of SSPF ice from above is determined by the energy input into the sediments. A measure for this energy input is the difference between the benthic temperature and the temperature of the upper sediment layer (ΔT). ΔT shows clear patterns when plotted against the local SIC (in time and space), Fig. 7. The local SIC sets a limit for ΔT, which is always essentially $0\,K$ when SIC $> 70\%$. With lower SIC the maximum "allowed" ΔT rises approximately linearly, independently of the chosen

190 scenario. The most $(\Delta T, SIC)$ points with low SIC are found in *pmt_ssp585*, but the relation for the maximum ΔT seems to be scenario-independent. This "universal" relation may explain the much larger SSPF melting in *pmt_ssp585* compared to the other scenarios.

4 Discussion

4.1 Relation between SSPF ice melting and sea ice

195 The rate of SSPF ice melting from above is determined largely by the benthic temperature (Fig. 7). The bentic temperature in turn is limited by the presence of sea ice which suppresses energy input into the ocean. Thus a direct relation can be found between the open sea season and the melting of SSPF ice (Figs. S9 and S10). A similar link was suggested by Dmitrenko et al. (2011) based on recent observed rise in the benthic temperatures on the East Siberian Shelf. In our model the link between absence of sea ice and melting of SSPF ice may be exaggered by the coarse resolution of MPI-OM implying a zero-curtain

200 effect on the sea ice/oceanic temperature relation on a relatively large scale. As long as a model grid cell has $SIC > 0$ all energy which goes into the ocean in this grid cell is used to melt the remaining sea ice, preventing a rise in the water temperature. In reality this is very dependent on the heterogeneity of the sea ice. If the remaining sea ice is collected in a corner of a the cell the water may be heated to above freezing point temperatures in the rest of the grid cell. Also the coarse MPI-OM resolution may underestimate the oceanic advection on the Arctic shelf, exaggerating the influence of sea ice on the SSPF on the local scale.

205 Despite these model artefacts, the basic physics of the causal relation chain from disappearance of sea ice to melting SSPF ice seems plausible.

4.2 Model limitations and assumptions

We are ignoring the thermal coupling between sea surface and the sediment at the sea bottom caused by bottom-fast ice (Nicolsky et al., 2012; Osterkamp et al., 1989), since such effects are, due to the coarse resolution of the ESM-setup of

210 JSBACH (Sec. 2.4), never relevant for a significant part of a grid point.

Freezing of the upper part of sub-sea sediment below shallow waters is in reality possible (Osterkamp et al., 1989), though this is mainly observed were bottom-fast ice is present. Due to the lack of diffusion of salt in the sediments in our model, we made the assumption that freezing of the below sea sediments is not happening, since in reality the salinity of the porewater

would be in equilibrium with the liquid sea water above. The validity of this assumption decreases with increasing depth
into the sediments due to the larger time lag of the salinity entrainment, caused by the difference between temperature and
salinity diffusivites (Harrison and Osterkamp, 1978)). We tested the consequences of this assumption by a series of sensitivity
experiments (Tabel 1, bottom) allowing the entire sediment column (*pmt_freeze* and *pmt_freeze126*) or the sediment below
$30\,cm$ (from layer 4 downward) to freeze (*pmt_fr3*). These experiments shows that freezing occurs mainly in the upper 2–3
layers (not shown). The water volume frozen (years 1850–3000) is 41, 170 and $12\,km^3$ for the three experiments respectively.
This is very small compared to the total volume of SSPF ice ($\approx 90-150\cdot10^3\,km^3$). Due to the energy buffering effect of
the freezing/melting cycle in the upper layers, a much larger volume of SSPF ice is preserved: $2.5\cdot10^3\,km^3$ less SSPF ice
melts by year 2000 (Fig. S8). For the strong forcing experiments (*pmt_freeze* and *pmt_fr3*) the difference to *pmt_ssp585*
is decreasing after year 2000 and is almost gone after year 2300. This "catching up" of the melting is facillitated by the
rising benthic temperatures which essentially prevents any freezing of sediments in the later part of these experiments. In
the low forcing experiment, *pmt_freeze126*, freezing takes place at an essentially constant rate throughout the experiments,
preserving the energy buffering in the upper layers. This results in a slight but persistently lower rate of SSPF ice melting than
in *pmt_ssp126*. In total, the difference to the main experiments is at most $\approx 2\%$ of the total SSPF ice volume. Based on these
sensitivity experiments, we conclude, that the influence of the "no re-freeze" assumption is minor and does not alter our main
conclusions. The "all-can-refreeze" and the main experiment bounds the realistic melting from below and above respectively.

In our setup, we suppress water advection in the unfrozen parts of the sediments. This is however unlikely to make any
difference for our main focus on the thawing from above, since the main effect is a heating from above which would tend to
stabilize the unfrozen sediment water column in the sediments. An active hydrology may however enhance the influcence of
the geothermal heating by increasing the effective upward heat flux.

On the Artic shelf, a broad range of sedimentation rates have been reported. From previous works, Overduin et al. (2019)
report rates from near zero to $700\,cm\,ka^{-1}$. For their model, they chose $30\,cm\,ka^{-1}$ for submerged points. Over the experi-
mental time of the present study, this would lead to a sedimentation of $\approx 34.5\,cm$ of additional sediment or $12\,cm$ during the
first 400 years of the experiments where the most interesting dynamics take place. Compared to a typical depth of ice melting
of at least $8\,m$ (Fig. 5) and the typical depth to which the seasonal temperature changes penetrates (30% of surface amplitude
at $\approx 4\,m$, Fig. S12), the added sediment is thus small and we therefore neglected sedimentation in the present study.

4.3 Area of SSPF

Our present day (2020) SSPF ice area, $\approx 2.74\cdot10^6\,km^2$, is larger than the SSPF area reported by Overduin et al. (2019),
$2.48\cdot10^6\,km^2$ which in turn is somewhat larger than the $\approx 2\cdot10^6\,km^2$ presented in Sayedi et al. (2020). Part of this difference
may be explained by Overduin et al. (2019) presenting a preindustrial estimate while Sayedi et al. (2020) refers to present-
day. In our model $\approx 0.15\cdot10^6\,km^2$ of SSPF ice area disappears during the 170 year period in between. These two studies
use the more common permafrost definition, based on continous years of sub-zero temperatures. If we apply this method, our
SSPF area is even larger: $3.31\cdot10^6\,km^2$ in 1850 ($3.18\cdot10^6\,km^2$ in 2020). That our SSPF area estimates are larger than the
previous studies is likely a result of the coarse T63 resolution causing extrapolation of SSPF to further off-shore locations (up

to $\approx 90\,km$) than included in the model of Overduin et al. (2019). A $90\,km$ wide stripe extending around the pole at $75°N$ has an area of $0.93 \cdot 10^6\,km^2$. Within this margin, our areas are in agreement with the other estimates.

250 ### 4.4 Geothermal heat flux and thawing rates (rate of change of IBPT)

The two sensitivity experiments excluding the geothermal heat flux (*pmt_pre_0* and *pmt_ssp585_0*) melt $4.7 \cdot 10^3\,km^3$ and $4.9 \cdot 10^3\,km^3$ ($4.0\,km^3\,a^{-1}$ and $4.2\,km^3\,a^{-1}$), respectively, less than the experiments with geothermal heat flux (Fig. S7). For *ssp_pre* this is more than half of the total melting, indicating that geothermal heat flux is more important than climate forcing for the melting. These two experiments represent the extremes of the forcing and since the geothermal melting is virtually
255 identical, it can be concluded that climate-caused melting from above and geothermally-caused melting from below are largely independent from each other and thus can be treated independently.

The rate of change of the IBPT controls the rate at which carbon become available for degradation. It can be roughly estimated by $\Delta IBPT = (T_{total} - T_{noheat})/\overline{por}$, where T_{total} and T_{noheat} are the SSPF ice melting rates in the main experment and the experiment without geothermal heat flux, respectively, and $\overline{por}$ is the average porosity over the layers where SSPF is
260 thawed. Assuming $\overline{por} = 0.35$ and ignoring the shrinking of SSPF area with time, the average $\Delta IBPT$ for points with SSPF ice is $0.8\,cm\,a^{-1}$, $0.9\,cm\,a^{-1}$, $1.2\,cm\,a^{-1}$, $1.7\,cm\,a^{-1}$ and $5.3\,cm\,a^{-1}$ for *pmt_pre*, *pmt_curr*, *pmt_ssp126*, *pmt_ssp245* and *pmt_ssp585* respectively for the 1850–3000 period. The $\Delta IBPT$ for the 1850–2009 period is $1.2\,cm\,a^{-1}$, and can be compared to present-day measurements. Overduin et al. (2015) measured thawing rates between 0 and $16\,cm\,a^{-1}$ off the Muostakh Island and Overduin et al. (2012) $0.5 - 1.4\,cm\,a^{-1}$ off Barrow. Both these study sites were in shallow waters very close to
265 the coast. The model hindcast study of Angelopoulos et al. (2019) presented thawing rates of $1.2 - 1.5\,cm\,a^{-1}$ and thus very similar to the rates found there. In the 22nd century peak of *pmt_ssp585* the thaw rate estimate is $11.4\,cm\,a^{-1}$.

5 Conclusions

Here, for the first time, a land component of an ESM was used to project the development of SSPF ice until year 3000 by forcing it with extended CMIP6 scenarios spanning the likely range of climate change. Using an ESM component has the advantage
270 over more specific SSPF models that it can be directly coupled to the carbon cycle to study climatic feedbacks. Though the inter-scenario differences are minor in the present century, in the 22nd century, the strong forcing scenario SSP5-8.5 strongly diverges by melting all SSPF ice above $\approx 100\,m$ depth, whereas the moderate and low forcing scenarios still leave SSPF ice below $\approx 8\,m$. This highlights the need to go beyond 2100, the usual time scale on which climate projections are made, to get the response of slowly acting climate components such as SSPF to a changing climate. The large loss of SSPF ice in SSP5-8.5
275 is closely linked to the disappearance of local sea ice. Specifically, the length of the open water season controls the temperature rise of the ocean water on the Arctic shelf. This temperature rise in turn determines the energy input into the ocean bottom sediments and thus the melting of SSPF ice. Therefore our results suggest, that the length of the local open water season may be used as an easy observable proxy for the rate of melting of SSPF ice.

Code availability. The MPI-ESM licenced model source code including the JSBACH version used for this study is stored in the git system of
280 MPI and will be made available by the first author on request. The running and plotting scripts are available together with the model output.

Data availability. https://cera-www.dkrz.de/WDCC/ui/cerasearch/entry?acronym=DKRZ_LTA_1142_ds00001

Author contributions. S. Wilkenskjeld made the current subsea implementation in JSBACH, decided on experiment setup, performed the
JSBACH experiments and subsequent analysis as well as being the main article writer, F. Miesner set up and performed the SuPerMAP
runs to create the initial data for JSBACH, P. Overduin supervised the SuPerMAP work and provided valuable discussion input, M. Puglini
285 made the initial subsea implementation (point model version) and the implementation of geothermal heat flux into JSBACH and V. Brovkin
provided initial ideas and supervised the work from start to end. All authors contributed to the writing.

Competing interests. The authors declare that they have no conflict of interest.

Acknowledgements. This study was funded by the EU-Horizon 2020 projects Nunataryuk, Grant-no: 773421, and CRESCENDO, Grant-no:
641816. The used model code is based on the version described in de Vrese et al. (2021) which was kindly provided by the Philipp de-Vrese
290 and the forcing data were kindly provided by Thomas Kleinen. Dirk Notz provided insights into the workings of the MPI-OM model.

References

Angelopoulos, M., Westermann, S., Overduin, P., Faguet, A., Olenchenko, V., Grosse, G., and Grigoriev, M. N.: Heat and Salt Flow in Subsea Permafrost Modeled with CryoGRID2, JOURNAL OF GEOPHYSICAL RESEARCH-EARTH SURFACE, 124, 920–937, https://doi.org/10.1029/2018JF004823, 2019.

295 Beven, K. J. and Kirkby, M. J.: A physically based, variable contributing area model of basin hydrology, Hydrological Sciences Bulletin, 24, 43–69, https://doi.org/10.1080/02626667909491834, 1979.

Brovkin, V., Ganopolski, A., Archer, D., and Munhoven, G.: Glacial CO2 cycle as a succession of key physical and biogeochemical processes, CLIMATE OF THE PAST, 8, 251–264, https://doi.org/10.5194/cp-8-251-2012, 2012.

Brovkin, V., Boysen, L., Arora, V. K., Boisier, J. P., Cadule, P., Chini, L., Claussen, M., Friedlingstein, P., Gayler, V., van den Hurk, B. J.

300 J. M., Hurtt, G. C., Jones, C. D., Kato, E., de Noblet-Ducoudre, N., Pacifico, F., Pongratz, J., and Weiss, M.: Effect of Anthropogenic Land-Use and Land-Cover Changes on Climate and Land Carbon Storage in CMIP5 Projections for the Twenty-First Century, JOURNAL OF CLIMATE, 26, 6859–6881, https://doi.org/10.1175/JCLI-D-12-00623.1, 2013.

Davies, J. H.: Global map of solid Earth surface heat flow, GEOCHEMISTRY GEOPHYSICS GEOSYSTEMS, 14, 4608–4622, https://doi.org/10.1002/ggge.20271, 2013.

305 de Vrese, P., Stacke, T., Kleinen, T., and Brovkin, V.: Diverging responses of high-latitude CO_2 and CH_4 emissions in idealized climate change scenarios, The Cryosphere, 15, 1097–1130, https://doi.org/10.5194/tc-15-1097-2021, 2021.

Dmitrenko, I. A., Kirillov, S. A., Tremblay, L. B., Kassens, H., Anisimov, O. A., Lavrov, S. A., Razumov, S. O., and Grigoriev, M. N.: Recent changes in shelf hydrography in the Siberian Arctic: Potential for subsea permafrost instability, JOURNAL OF GEOPHYSICAL RESEARCH-OCEANS, 116, https://doi.org/10.1029/2011JC007218, 2011.

310 Ekici, A., Beer, C., Hagemann, S., Boike, J., Langer, M., and Hauck, C.: Simulating high-latitude permafrost regions by the JSBACH terrestrial ecosystem model, Geoscientific Model Development, 7, 631–647, https://doi.org/10.5194/gmd-7-631-2014, 2014.

Eyring, V., Bony, S., Meehl, G. A., Senior, C. A., Stevens, B., Stouffer, R. J., and Taylor, K. E.: Overview of the Coupled Model Intercomparison Project Phase 6 (CMIP6) experimental design and organization, Geoscientific Model Development, 9, 1937–1958, https://doi.org/10.5194/gmd-9-1937-2016, 2016.

315 Giorgetta, M. A., Jungclaus, J., Reick, C. H., Legutke, S., Bader, J., Böttinger, M., Brovkin, V., Crueger, T., Esch, M., Fieg, K., Glushak, K., Gayler, V., Haak, H., Hollweg, H.-D., Ilyina, T., Kinne, S., Kornblueh, L., Matei, D., Mauritsen, T., Mikolajewicz, U., Mueller, W., Notz, D., Pithan, F., Raddatz, T., Rast, S., Redler, R., Roeckner, E., Schmidt, H., Schnur, R., Segschneider, J., Six, K. D., Stockhause, M., Timmreck, C., Wegner, J., Widmann, H., Wieners, K.-H., Claussen, M., Jochem, M., and Stevens, B.: Climate and carbon cycle changes from 1850 to 2100 in MPI-ESM simulations for the coupled model intercomparison project phase 5, Journal of advances in modeling

320 earth systems, 5, 572–597, https://doi.org/10.1002/jame.20038, 2013.

Goll, D. S., Brovkin, V., Liski, J., Raddatz, T., Thum, T., and Todd-Brown, K. E. O.: Strong dependence of CO2 emissions from anthropogenic land cover change on initial land cover and soil carbon parametrization, GLOBAL BIOGEOCHEMICAL CYCLES, 29, 1511–1523, https://doi.org/10.1002/2014GB004988, 2015.

Hagemann, S. and Stacke, T.: Impact of the soil hydrology scheme on simulated soil moisture memory, CLIMATE DYNAMICS, 44, 1731–

325 1750, https://doi.org/10.1007/s00382-014-2221-6, 2015.

Harrison, W. and Osterkamp, T.: Heat and mass transport processes in subsea permafrost 1. An analysis of molecular diffusion and its consequences, Journal of Geophysical Research, 83, 4707–4712, https://doi.org/10.1029/JC083iC09p04707, 1978.

Hugelius, G., Strauss, J., Zubrzycki, S., Harden, J. W., Schuur, E. A. G., Ping, C. L., Schirrmeister, L., Grosse, G., Michaelson, G. J., Koven, C. D., O'Donnell, J. A., Elberling, B., Mishra, U., Camill, P., Yu, Z., Palmtag, J., and Kuhry, P.: Estimated stocks of circumpolar permafrost carbon with quantified uncertainty ranges and identified data gaps, BIOGEOSCIENCES, 11, 6573–6593, https://doi.org/10.5194/bg-11-6573-2014, 2014.

Kleinen, T. and Brovkin, V.: Pathway-dependent fate of permafrost region carbon, Environmental Research Letters, 13, https://doi.org/10.1088/1748-9326/aad824, 2018.

Kleinen, T., Gromov, S., Steil, B., and Brovkin, V.: CMIP6 underestimates future Methane, Submitted to Environmental Research Letters, 2021.

Kleinen, T., Brovkin, V., and Munhoven, G.: Modelled interglacial carbon cycle dynamics during the Holocene, the Eemian and Marine Isotope Stage (MIS) 11, CLIMATE OF THE PAST, 12, 2145–2160, https://doi.org/10.5194/cp-12-2145-2016, 2016.

Kleinen, T., Mikolajewicz, U., and Brovkin, V.: Terrestrial methane emissions from the Last Glacial Maximum to the preindustrial period, CLIMATE OF THE PAST, 16, 575–595, https://doi.org/10.5194/cp-16-575-2020, 2020.

Koven, C. D., Schuur, E. A. G., Schaedel, C., Bohn, T. J., Burke, E. J., Chen, G., Chen, X., Ciais, P., Grosse, G., Harden, J. W., Hayes, D. J., Hugelius, G., Jafarov, E. E., Krinner, G., Kuhry, P., Lawrence, D. M., MacDougall, A. H., Marchenko, S. S., McGuire, A. D., Natali, S. M., Nicolsky, D. J., Olefeldt, D., Peng, S., Romanovsky, V. E., Schaefer, K. M., Strauss, J., Treat, C. C., and Turetsky, M.: A simplified, data-constrained approach to estimate the permafrost carbon-climate feedback, PHILOSOPHICAL TRANSACTIONS OF THE ROYAL SOCIETY A-MATHEMATICAL PHYSICAL AND ENGINEERING SCIENCES, 373, https://doi.org/10.1098/rsta.2014.0423, 2015.

Lawrence, D. M., Fisher, R. A., Koven, C. D., Oleson, K. W., Swenson, S. C., Bonan, G., Collier, N., Ghimire, B., van Kampenhout, L., Kennedy, D., Kluzek, E., Lawrence, P. J., Li, F., Li, H., Lombardozzi, D., Riley, W. J., Sacks, W. J., Shi, M., Vertenstein, M., Wieder, W. R., Xu, C., Ali, A. A., Badger, A. M., Bisht, G., van den Broeke, M., Brunke, M. A., Burns, S. P., Buzan, J., Clark, M., Craig, A., Dahlin, K., Drewniak, B., Fisher, J. B., Flanner, M., Fox, A. M., Gentine, P., Hoffman, F., Keppel-Aleks, G., Knox, R., Kumar, S., Lenaerts, J., Leung, L. R., Lipscomb, W. H., Lu, Y., Pandey, A., Pelletier, J. D., Perket, J., Randerson, J. T., Ricciuto, D. M., Sanderson, B. M., Slater, A., Subin, Z. M., Tang, J., Thomas, R. Q., Martin, M. V., and Zeng, X.: The Community Land Model Version 5: Description of New Features, Benchmarking, and Impact of Forcing Uncertainty, JOURNAL OF ADVANCES IN MODELING EARTH SYSTEMS, 11, 4245–4287, https://doi.org/10.1029/2018MS001583, 2019.

Malakhova, V. V. and Eliseev, V, A.: Salt diffusion effect on the submarine permafrost state and distribution as well as on the stability zone of methane hydrates on the Laptev Sea shelf, LED I SNEG-ICE AND SNOW, 60, 533–546, https://doi.org/10.31857/S2076673420040058, 2020.

Mauritsen, T., Bader, J., Becker, T., Behrens, J., Bittner, M., Brokopf, R., Brovkin, V., Claussen, M., Crueger, T., Esch, M., Fast, I., Fiedler, S., Flaeschner, D., Gayler, V., Giorgetta, M., Goll, D. S., Haak, H., Hagemann, S., Hedemann, C., Hohenegger, C., Ilyina, T., Jahns, T., Jimenez-de-la Cuesta, D., Jungclaus, J., Kleinen, T., Kloster, S., Kracher, D., Kinne, S., Kleberg, D., Lasslop, G., Kornblueh, L., Marotzke, J., Matei, D., Meraner, K., Mikolajewicz, U., Modali, K., Moebis, B., Muellner, W. A., Nabel, J. E. M. S., Nam, C. C. W., Notz, D., Nyawira, S.-S., Paulsen, H., Peters, K., Pincus, R., Pohlmann, H., Pongratz, J., Popp, M., Raddatz, T. J., Rast, S., Redler, R., Reick, C. H., Rohrschneider, T., Schemann, V., Schmidt, H., Schnur, R., Schulzweida, U., Six, K. D., Stein, L., Stemmler, I., Stevens, B., von Storch, J.-S., Tian, F., Voigt, A., Vrese, P., Wieners, K.-H., Wilkenskjeld, S., Winkler, A., and Roeckner, E.: Developments in the MPI-M Earth System Model version 1.2 (MPI-ESM1.2) and Its Response to Increasing CO2, JOURNAL OF ADVANCES IN MODELING EARTH SYSTEMS, 11, 998–1038, https://doi.org/10.1029/2018MS001400, 2019.

365   McGuire, A. D., Lawrence, D. M., Koven, C., Clein, J. S., Burke, E., Chen, G., Jafarov, E., MacDougall, A. H., Marchenko, S., Nicolsky, D., Peng, S., Rinke, A., Ciais, P., Gouttevin, I., Hayes, D. J., Ji, D., Krinner, G., Moore, J. C., Romanovsky, V., Schaedel, C., Schaefer, K., Schuur, E. A. G., and Zhuang, Q.: Dependence of the evolution of carbon dynamics in the northern permafrost region on the trajectory of climate change, PROCEEDINGS OF THE NATIONAL ACADEMY OF SCIENCES OF THE UNITED STATES OF AMERICA, 115, 3882–3887, https://doi.org/10.1073/pnas.1719903115, 2018.

370   Meinshausen, M., Nicholls, Z. R. J., Lewis, J., Gidden, M. J., Vogel, E., Freund, M., Beyerle, U., Gessner, C., Nauels, A., Bauer, N., Canadell, J. G., Daniel, J. S., John, A., Krummel, P. B., Luderer, G., Meinshausen, N., Montzka, S. A., Rayner, P. J., Reimann, S., Smith, S. J., van den Berg, M., Velders, G. J. M., Vollmer, M. K., and Wang, R. H. J.: The shared socio-economic pathway (SSP) greenhouse gas concentrations and their extensions to 2500, Geoscientific Model Development, 13, 3571–3605, https://doi.org/10.5194/gmd-13-3571-2020, 2020.

Nicolsky, D. and Shakhova, N.: Modeling sub-sea permafrost in the East Siberian Arctic Shelf: the Dmitry Laptev Strait, ENVIRONMEN-
375   TAL RESEARCH LETTERS, 5, https://doi.org/10.1088/1748-9326/5/1/015006, 2010.

Nicolsky, D. J., Romanovsky, V. E., Romanovskii, N. N., Kholodov, A. L., Shakhova, N. E., and Semiletov, I. P.: Modeling sub-sea permafrost in the East Siberian Arctic Shelf: The Laptev Sea region, JOURNAL OF GEOPHYSICAL RESEARCH-EARTH SURFACE, 117, https://doi.org/10.1029/2012JF002358, 2012.

Osterkamp, T., Baker, G., Harrison, W., and Matava, T.: Characteristics of the Active Layer and Shallow Subsea Permafrost, Journal of
380   Geophysical Research-Oceans, 94, 16 227–16 236, https://doi.org/10.1029/JC094iC11p16227, 1989.

Overduin, P., Westermann, S., Yoshikawa, K., Haberlau, T., Romanovsky, V., and Wetterich, S.: Geoelectric observations of the degradation of nearshore submarine permafrost at Barrow (Alaskan Beaufort Sea), Journal of Geophysical Research, 117, https://doi.org/10.1029/2011JF002088, 2012.

Overduin, P. P., Haberland, C., Ryberg, T., Kneier, F., Jacobi, T., Grigoriev, M. N., and Ohrnberger, M.: Submarine permafrost depth from
385   ambient seismic noise, Geophysical Research Letters, 42, 7581–7588, https://doi.org/10.1002/2015GL065409, 2015.

Overduin, P. P., Schneider von Deimling, T., Miesner, F., Grigoriev, M. N., Ruppel, C., Vasiliev, A., Lantuit, H., Juhls, B., and Westermann, S.: Submarine Permafrost Map in the Arctic Modeled Using 1-D Transient Heat Flux (SuPerMAP), Journal of Geophysical Research: Oceans, 0, https://doi.org/10.1029/2018JC014675, 2019.

Petoukhov, V., Ganopolski, A., Brovkin, V., Claussen, M., Eliseev, A., Kubatzki, C., and Rahmstorf, S.: CLIMBER-2: a climate system
390   model of intermediate complexity. Part I: model description and performance for present climate, CLIMATE DYNAMICS, 16, 1–17, https://doi.org/10.1007/PL00007919, 2000.

Reick, C. H., Raddatz, T., Brovkin, V., and Gayler, V.: Representation of natural and anthropogenic land cover change in MPI-ESM, Journal of advances in modeling earth systems, 5, 459–482, https://doi.org/10.1002/jame.20022, 2013.

Riley, W. J., Subin, Z. M., Lawrence, D. M., Swenson, S. C., Torn, M. S., Meng, L., Mahowald, N. M., and Hess, P.: Barriers to pre-
395   dicting changes in global terrestrial methane fluxes: analyses using CLM4Me, a methane biogeochemistry model integrated in CESM, Biogeosciences, 8, 1925–1953, https://doi.org/10.5194/bg-8-1925-2011, 2011.

Sayedi, S. S., Abbott, B. W., Thornton, B. F., Frederick, J. M., Vonk, J. E., Overduin, P., Schädel, C., Schuur, E. A. G., Bourbonnais, A., Demidov, N., Gavrilov, A., He, S., Hugelius, G., Jakobsson, M., Jones, M. C., Joung, D., Kraev, G., Macdonald, R. W., McGuire, A. D., Mu, C., O'Regan, M., Schreiner, K. M., Stranne, C., Pizhankova, E., Vasiliev, A., Westermann, S., Zarnetske, J. P., Zhang, T., Ghandehari,
400   M., Baeumler, S., Brown, B. C., and Frei, R. J.: Subsea permafrost carbon stocks and climate change sensitivity estimated by expert assessment, Environmental Research Letters, 15, 124 075, https://doi.org/10.1088/1748-9326/abcc29, 2020.

Schulzweida, U.: CDO User Guide, https://doi.org/10.5281/zenodo.3539275, 2019.

Schuur, E. A. G., McGuire, A. D., Schaedel, C., Grosse, G., Harden, J. W., Hayes, D. J., Hugelius, G., Koven, C. D., Kuhry, P., Lawrence, D. M., Natali, S. M., Olefeldt, D., Romanovsky, V. E., Schaefer, K., Turetsky, M. R., Treat, C. C., and Vonk, J. E.: Climate change and the

405   permafrost carbon feedback, NATURE, 520, 171–179, https://doi.org/10.1038/nature14338, 2015.

Shakhova, N. E., Nicolsky, D. Y., and Semiletov, I. P.: Current state of subsea permafrost on the East Siberian Shelf: Tests of modeling results based on field observations, DOKLADY EARTH SCIENCES, 429, 1518–1521, https://doi.org/10.1134/S1028334X09090220, 2009.

Tuomi, M., Thum, T., Jarvinen, H., Fronzek, S., Berg, B., Harmon, M., Trofymow, J. A., Sevanto, S., and Liski, J.: Leaf litter decomposition-Estimates of global variability based on Yasso07 model, ECOLOGICAL MODELLING, 220, 3362–3371,

410   https://doi.org/10.1016/j.ecolmodel.2009.05.016, 2009.

Turetsky, M. R., Abbott, B. W., Jones, M. C., Anthony, K. W., Olefeldt, D., Schuur, E. A. G., Grosse, G., Kuhry, P., Hugelius, G., Koven, C., Lawrence, D. M., Gibson, C., Sannel, A. B. K., and McGuire, A. D.: Carbon release through abrupt permafrost thaw, NATURE GEOSCIENCE, 13, 138+, https://doi.org/10.1038/s41561-019-0526-0, 2020.
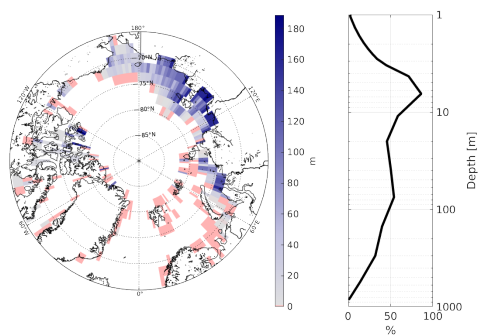
Figure 1. *(Left)* Length of initial (1850) SSPF ice column. Redish color mark points entirely without ice in the sediments. *(Right)* Vertical distribution of initial ice concentration in sediment pore space (SSPF ice saturation). The right panel shows the spatial average over the area containing SSPF ice in 1850.
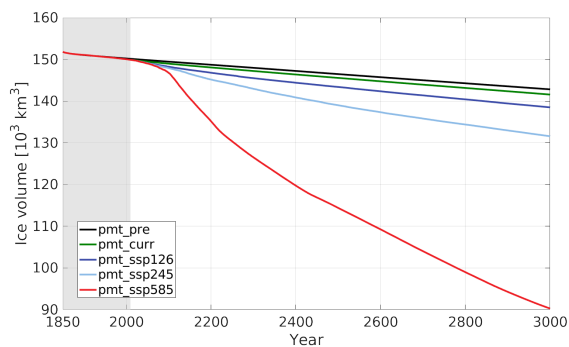
Figure 2. Volume of pan-Artic SSPF ice for the scenario and control experiments. Gray shading marks the historical period.
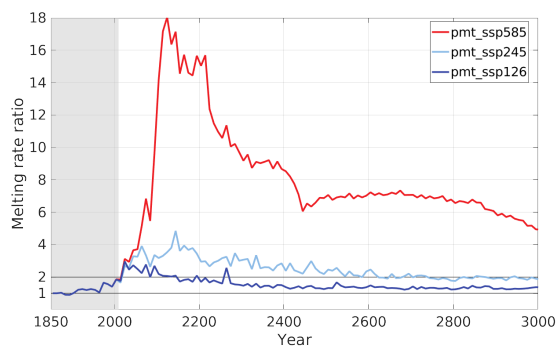
Figure 3. Melting rate ratios relative to *pmt_pre* for the main scenarios. 10 year averages. Gray shading marks the historical period.
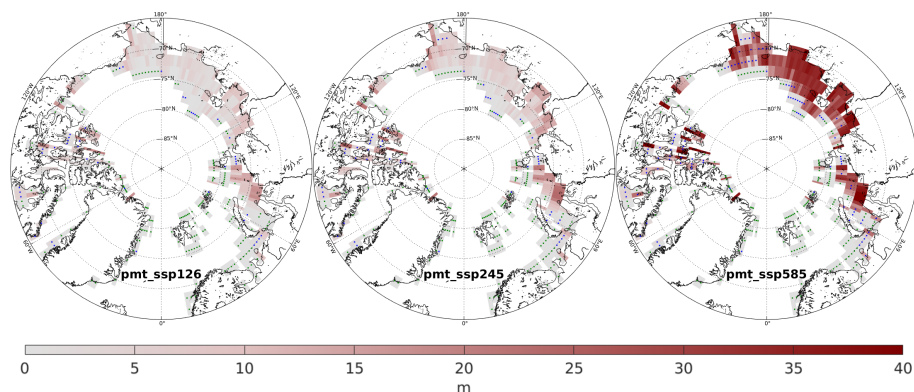
Figure 4. SSPF ice column melting for the three main experiments in the period 1850–3000. Green dots mark points entirely without SSPF ice and blue mark points where all SSPF ice melted before year 3000.
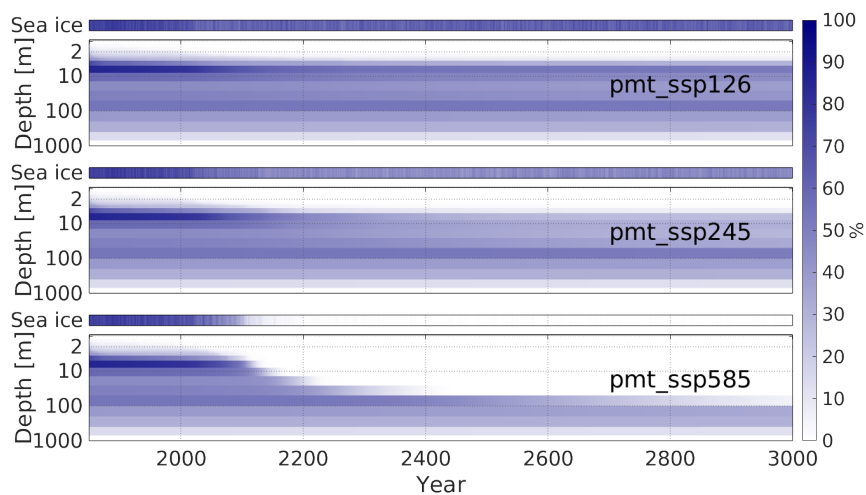
Figure 5. Vertical distribution of SSPF ice saturation (main panels) and sea ice concentration (top panels) for the scenario experiments. Yearly averages for the 242 points which contained ice in the initial conditions (1850).
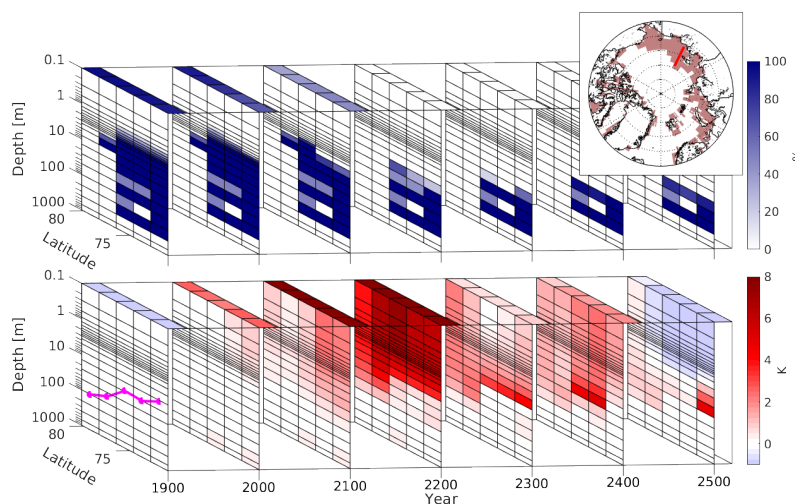
Figure 6. SSPF ice saturation (upper panel, *lat/depth*-planes), sea ice concentration (upper panel, *lat/year*-plane), sediment temperature change (lower panel, *lat/depth*-planes) and atmospheric $2\,m$ temperature change (lower panel, *lat/time*-plane) along a section across the East Siberian Shelf ($153°E$, shown on the insert in the upper panel) for different time periods. In the lower panel time slice at 1900 represent the 1850–1900 change, the remaining the changes relative to the slice before. Black lines at constant depth are model layer boundaries. Magenta line shows the water depth along the section. Shown are (differences between) yearly averages.
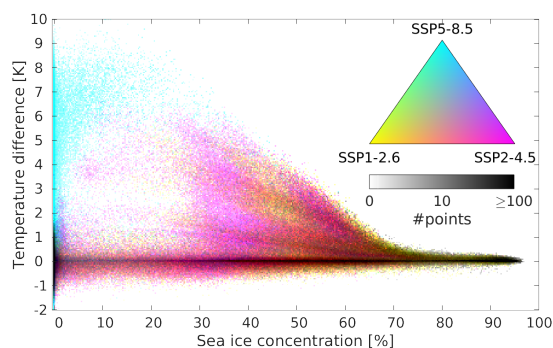
Figure 7. Temperature difference between ocean bottom and upper sub-sea sediment as function of local sea ice concentration for the scenario experiments. Logarithmic density plot (temperature difference in $0.05\,K$ bins, sea ice cover in 0.25% bins) of monthly values. The colors are combined RGB-wise according to the color triangle. The color saturation is scaled such that 0 points in a bin corresponds to the value 0 and ≥ 100 points corresponds to the value 1. Thus for instance a red point contains equally many points from *pmt_ssp126* and *pmt_ssp245* but none from *pmt_ssp585*. Black indicate at least 100 points in all three scenarios. Each scenario contributes more than 460,000 time-space points.

Table 1. Performed experiments. The forcing for the three SSPs is identical for the period 1850–2009. *: Forcing repeated cyclicly. "Geoth": Geothermal heat flux included? "Freezing layers": Freezing of porewater allowed for these layers.

Experiment	Purpose	Period	Forcing	Forcing period	Geoth	Freezing layers	Restart @year
pmt_ssp126	main	1850-3299	ssp1-2.6	1850-3299	Yes	None	
pmt_ssp245	main	1850-3309	ssp2-4.5	1850-3309	Yes	None	
pmt_ssp585	main	1850-3169	ssp5-8.5	1850-3169	Yes	None	
pmt_pre	control	1850-3109	ssp1-2.6	1850-1873*	Yes	None	
pmt_curr	control	2010-3109	ssp1-2.6	1986-2009*	Yes	None	pmt_ssp126 2010
pmt_pre_0	sensitivity	1850-3109	ssp1-2.6	1850-1873*	No	None	
pmt_ssp585_0	sensitivity	1850-3169	ssp5-8.5	1850-3169	No	None	
pmt_freeze126	sensitivity	1850-3169	ssp1-2.6	1850-3169	Yes	1–22 (all)	
pmt_freeze	sensitivity	1850-3169	ssp5-8.5	1850-3169	Yes	1–22 (all)	
pmt_fr3	sensitivity	1850-3169	ssp5-8.5	1850-3169	Yes	4–22	

Table 2. Overview over volume (left) and area (right) of SSPF ice in the main and control experiments at selected times. Numbers in brackets indicate relative loss compared to 1850.

	Volume $10^3\,km^3$ (%)					Area $10^6\,km^2$ (%)				
Year	1850	2100	2200	2500	3000	1850	2100	2200	2500	3000
Experiment										
pmt_pre	153	149 (2.1)	149 (2.6)	147 (4.1)	143 (6.5)	2.89	2.74 (5.0)	2.71 (6.1)	2.68 (7.3)	2.63 (8.9)
pmt_curr	153	149 (2.4)	148 (3.0)	146 (4.7)	142 (7.3)	2.89	2.72 (5.7)	2.68 (7.0)	2.60 (9.9)	2.55 (11.8)
pmt_ssp126	153	148 (2.9)	147 (3.9)	143 (6.1)	139 (9.3)	2.89	2.64 (8.5)	2.53 (12.2)	2.41 (16.5)	2.37 (17.8)
pmt_ssp245	153	148 (3.1)	145 (4.9)	139 (9.0)	132 (13.8)	2.89	2.61 (9.6)	2.38 (17.6)	2.27 (21.3)	2.22 (23.1)
pmt_ssp585	153	147 (3.9)	135 (11.5)	114 (25.1)	90 (40.9)	2.89	2.53 (12.3)	2.21 (23.3)	2.03 (29.7)	1.65 (42.7)